Article:
Chau, C.C.C. orcid.org/0000-0002-3134-6798, Weckman, N.E. orcid.org/0000-0001-5894-4926, Thomson, E.E. orcid.org/0000-0002-0266-7090 et al. (1 more author) (2025) Solid-state nanopore real-time assay for monitoring Cas9 endonuclease reactivity. ACS Nano, 19 (3). pp. 3839-3851. ISSN 1936-0851

https://doi.org/10.1021/acsnano.4c15173

ACS NANO

www.acsnano.org

ARTICLE

Solid-State Nanopore Real-Time Assay for Monitoring Cas9 Endonuclease Reactivity

Chalmers C. C. Chau,* Nicole E. Weckman, Emma E. Thomson, and Paolo Actis

Cite This: *ACS Nano* 2025, 19, 3839−3851

Read Online

ACCESS | Metrics & More | Article Recommendations | Supporting Information

ABSTRACT: **The field of nanopore sensing is now moving beyond nucleic acid sequencing. An exciting avenue is the use of nanopore platforms for the monitoring of biochemical reactions. Biological nanopores have been used for this application, but solid-state nanopore approaches have lagged. This is due to the necessity of using higher salt conditions (e.g., 4 M LiCl) to improve the signal-to-noise ratio which completely abolish the activities of many biochemical reactions. We pioneered a polymer electrolyte solid-state nanopore approach that maintains a high signal-to-noise ratio even at a physiologically relevant salt concentration. Here, we report the monitoring of the restriction enzyme SwaI and CRISPR-Cas9 endonuclease activities under physiological salt conditions and in real time. We investigated the dsDNA cleavage activity of these enzymes in a range of digestion buffers and elucidated the off-target activity of CRISPR-Cas9 ribonucleoprotein endonuclease in the presence of single base pair mismatches. This approach enables the application of solid-state nanopores for the dynamic monitoring of biochemical reactions under physiological salt conditions.**

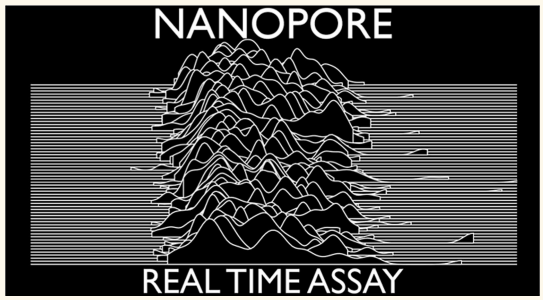

KEYWORDS: *nanopore, endonuclease, CRISPR, single molecule, polymer electrolyte*

INTRODUCTION

Single molecule analysis is advancing the understanding of fundamental biochemical and biophysical processes involving DNA, RNA, proteins, and cellular machinery.[1−3] Numerous tools have been developed for single molecule analysis such as atomic force microscopy,[4] super resolution fluorescent microscopy,[5] optical tweezers,[6] and single molecule Förster resonance energy transfer (sm-FRET).[7] Unlike many of these techniques that require fluorescent or chemical labeling of the analyte, nanopore sensors are a label-free single molecule analysis technique amenable to high throughput analyses.[3,8,9] Nanopores are utilized for the sequencing of nucleic acids[10] but have also been extensively used for the biophysical characterization of a range of biomolecules.[11−18] In a nanopore experiment, an analyte passes through the nanopore with the application of an electric field. This elicits a temporary modulation of the measured ion current through the pore, which depends on the volume and surface charge of the translocating analyte.[15] Nanopores are best known for their commercial application for sequencing nucleic acids;[10] however, they are broadly useful for the biophysical characterization of a range of biomolecules and their interactions.[11−15] Furthermore, nanopores provide real-time detection of analytes, which makes them ideal as a technique to monitor reactions[19,20] or investigate biochemical processes such as monitoring enzymatic activity.[19−23]

Enzymes such as endonucleases are biological catalysts of chemical reactions and play a major role in physiological processes and in synthetic biology,[24] and biological nanopores have been used to investigate the dynamics of enzymatic reactions.[22,23,25−28] The investigation of enzymatic reactions with biological pores often relies on immobilization of the enzyme at the nanopore or confinement of the enzyme in the pore.[19−21] The size of solid-state nanopores can be easily tuned, allowing for the direct study of both products of enzymatic reactions as well as the enzyme−substrate interactions without immobilization or confinement of the enzyme.[29−33] However, the use of solid-state nanopores to monitor enzymatic reactions has been limited, due to the need of using high electrolyte conditions (e.g., 4 M LiCl) to improve the signal-to-noise ratio.[29−32,34,35] As most enzymes are only catalytically active under a specific salt concentration, these high salt conditions do not allow for the real-time monitoring of enzymatic activities.

Received: October 25, 2024
Revised: December 12, 2024
Accepted: December 19, 2024
Published: January 15, 2025

Here, we overcome this challenge by using a polymer electrolyte to enhance the nanopore sensing performance while still enabling measurements in physiologically relevant conditions.[36−40] We demonstrate the capabilities of this system for monitoring the digestion activities of two distinct sequence specific endonucleases: restriction enzyme SwaI and CRISPR-Cas9. We develop and optimize the real-time quantitative analysis system using a well-understood restriction endonuclease, SwaI. We then demonstrate the proof-of-principle of real-time quantitative analysis of CRISPR-Cas9 on-target and off-target endonuclease activity, an understanding of which is critically important for applications in gene therapy or the wider biotechnology applications of CRISPR-Cas9 approaches.

With further development and optimization, we envision that we can apply our solid-state nanopore kinetic measurement system beyond monitoring endonuclease activities, with many potential uses for monitoring assembly and disassembly of larger biological complexes. The tunable pore size of our system opens the door to a broad range of applications studying biomolecules of various sizes, like facilitating the detection of protein aggregation.[36,41−43]

RESULTS AND DISCUSSION

Real-Time Quantitative Nanopore Analysis System for Endonuclease. We designed a 3 kbp dsDNA (RS-dsDNA) with a restriction site for the restriction enzyme SwaI at its center,[44] and designed the on- and off-target crRNA variants for the CRISPR-Cas9 digestion system to perform digestion at the center of the RS-dsDNA.[45] The successful digestion of the RS-dsDNA by either enzyme means the cleavage of the 3 kbp RS-dsDNA, resulting in the production of two 1.5 kbp dsDNA fragments. Our solid-state nanopore system can clearly distinguish the sizes of these dsDNA[40] based on peak amplitude of the translocation event and can monitor changes in the population of these cleaved RS-dsDNA in real time. For the SwaI endonuclease activity, we investigated the effect of the buffer composition and showed that suboptimal buffer composition abolished enzyme activities, in agreement with gel electrophoresis data. For CRISPR-Cas9, we studied the effects of sequence mismatches between the crRNA and target DNA sequence on the endonuclease activity. Mismatches led to slower cleavage activities, and our system indicates that mismatches at positions 1 and 4 upstream of the protospacer adjacent motif (PAM) site significantly reduced the cleavage activities.

We recently developed a method to enhance the performance of a glass solid-state nanopore, by replacing the electrolyte bath (trans chamber) with a polymer electrolyte bath composed of 50% (w/v) poly(ethylene) glycol (PEG) and 0.1 M KCl.[36−40] Unlike other solid-state nanopore systems, where the dsDNA separation relies on the event dwell time and the current signal is resistive,[46−48] our setup produces a conductive pulse as molecules translocate from the cis chamber (inside the nanopore) to the trans chamber (outside the nanopore). Using these conductive translocation signals, we previously showed that dsDNA fragments of different lengths (0.7 to 7 kbp) can be reliably detected and distinguished.[40]

Crucially, the system's sensitivity depends only on the electrolyte property in the trans chamber bath, while the electrolyte property in the cis chamber, where the analyte is placed, has minimal effect on the signal-to-noise ratio.[37,39,40] The combination of the polymer electrolyte in the trans chamber and the standard electrolyte (e.g., 0.1 M KCl) in the cis chamber forms a physical interface at the nanopore aperture. When dsDNA translocates through the nanopore from the cis to trans chamber, this interface is mechanically disrupted, causing ions to accumulate and leading to an enhanced conductivity in the system; the extent of this disruption is directly proportional to the length of the dsDNA.[40] This unique property allows the measurement to be performed at near or lower than physiological salt concentrations without compromising the single-molecule sensitivity. Additionally, the system can operate continuously for at least 30 min without any noticeable change in performance.[40]

The glass nanopore used here has a diameter of approximately 70 nm (Figure S1) and its response is highly reproducible as demonstrated by $I-V$ measurements (Figure S2), indicating the precise control on the fabrication of the nanopore.

Through modern synthetic biochemistry and molecular cloning techniques[49] (Figures 1A and S3), we generated the 3 kbp dsDNA (RS-dsDNA) containing a specific restriction site (5′-ATTT/AAAT-3′) at the center of the RS-dsDNA, which allows the restriction enzyme SwaI to digest it into 2 pieces of 1.5 kbp dsDNA,[44] as shown in Figure 1B.

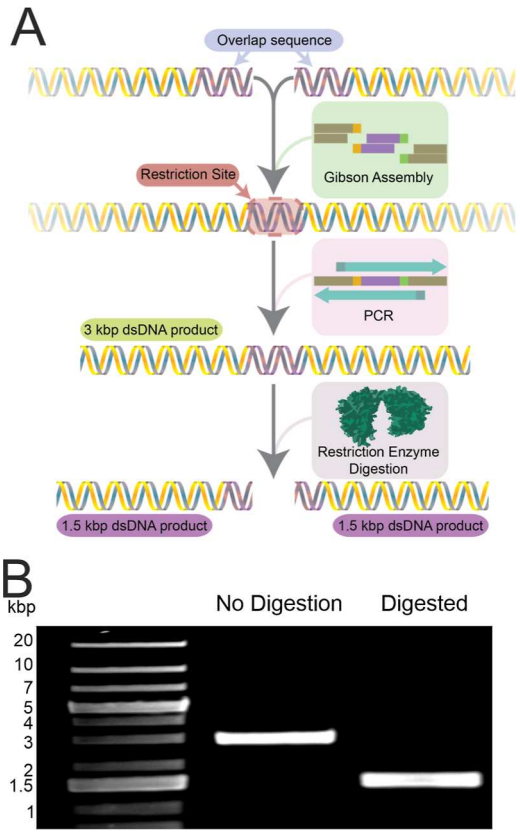

Figure 1. Generation of the restriction site containing 3 kbp dsDNA. (A) Schematic illustration of the generation of the restriction site containing 3 kbp dsDNA (RS-dsDNA). (B) Agarose gel electrophoresis analysis of the undigested RS-dsDNA and the digested RS-dsDNA; the 3 kbp original fragment was digested into 1.5 kbp dsDNA.

We performed translocation of dsDNA of different sizes into the polymer electrolyte bath and observed that dsDNA of

https://doi.org/10.1021/acsnano.4c15173
ACS Nano 2025, 19, 3839−3851

distinct sizes could be classified based on their peak amplitudes[37,40] (Figure S4A). We tested the translocation of the purified RS-dsDNA under different voltages (Figure S4B) and we selected −700 mV for the rest of the study, as it provided a suitable capture rate to facilitate statistical analyses. Similarly, the optimal concentration of the RS-dsDNA was determined after screening a range of concentrations (Figure S4C). Next, we tested the ability of the system to distinguish the SwaI digested (1.5 kbp) and undigested RS-dsDNA (3.0 kbp). Prior to the experiment, the RS-dsDNA was digested with the restriction enzyme SwaI and the products were purified and diluted down to 10 nM with 0.1 M KCl. We observed translocation signals for both the RS-dsDNA and the digested RS-dsDNA (Figure S4D). The population scatter showed the major population shift from a higher current amplitude to a lower current amplitude after digestion, in line with our previous observations.[40] The current peak amplitude of the single molecule translocation events of the undigested RS-dsDNA formed a population at about 0.3 nA while the digested RS-dsDNA formed a population at about 0.2 nA (Figure S4E) demonstrating that the peak amplitude can be used a discriminant to separate the two populations (Figure S4F). Due to the dimension of the nanopore used here (Figure S1), the translocation of the restriction enzyme could not be detected (Figure S5).

The detection of dsDNA translocating through a solid-state nanopore at high resolution has been reported extensively before, but most experiments are carried out at higher than physiological salt concentration (e.g., 0.5 to 4 M) and with a monovalent salt like LiCl that is not commonly found in physiological conditions.[50−63] However, performing single molecule detection with solid-state nanopores at high salt conditions can hinder or suppress the activity of restriction enzymes. Most routinely used digestion buffers contain 50 to 100 mM of NaCl (Table 1) and increasing the concentration

Table 1. Composition of Digestion Buffers

buffer name	composition
buffer 3.1	50 mM Tris−HCl, 10 mM $MgCl_2$, 100 mM NaCl, 100 μg/mL BSA at pH 7.9
buffer 4	20 mM Tris-OAc, 10 mM MgOAc, 50 mM KOAc, 1 mM DTT, pH 7.9
buffer 2.1	50 mM Tris−HCl, 10 mM $MgCl_2$, 50 mM NaCl, 100 μg/mL BSA, pH 7.9
CutSmart	20 mM Tris-OAc, 10 mM MgOAc, 50 mM KOAc, 100 μg/mL BSA, pH 7.9

of NaCl to 1 M completely abolishes the SwaI activity (Figure S7A). The high dependency on the salt concentration makes enzyme activities difficult to monitor using solid-state nanopores. Additionally, we observed that the application of voltage has no effect on the digestion ability of the enzymes (Figure S7B).

To overcome this challenge, we leverage the benefits of the polymer electrolyte and developed an assay to monitor the dsDNA cleavage activities of the SwaI enzyme in real time. This is done by monitoring the gradual reduction in the number of RS-dsDNA translocation events over time as it gets cleaved by SwaI. To prevent potential clogging of the dsDNA at the nanopore over time, we applied a waveform composed of 3.5 s of +100 mV followed by 6 s of −700 mV (Figure S8). This waveform allows us to control the delivery of the dsDNA on demand as the dsDNA will migrate away from the nanopore due to the voltage polarity.[64] This waveform is looped 180 to 360 times (30 min to 1 h), allowing the real-time monitoring of the enzymatic reaction.

We first demonstrated that the digestion reaction carried out inside the glass nanopore capillary provides results comparable to those of the reaction performed in a standard reaction tube (Figure S9). Next, the mixture composed of 1× buffer 3.1 (Table 1), 10 nM RS-dsDNA, and 5 units of SwaI was prepared and immediately loaded into the cis chamber of the nanopore, which was then immersed in the polymer electrolyte followed by the application of the waveform described above (Figure 2A). The translocation events at 1, 10, 20 min and finally at 30 min were isolated, and 20 random events were overlapped as shown in Figure 2B, to show the visual progression of the reduction in the current peak amplitudes at different time points. Similarly, Figure 2C shows the population distribution of the translocation events at 1, 10, 20, and 30 min. The higher peak amplitude population was the major population at the 1 min time point, indicating the presence of the RS-dsDNA; this population slowly reduced at 10 and 20 min and finally only a minor population of the RS-dsDNA could be detected at 30 min.

The population shift could be difficult to capture through scatter plots, so we used ridgeline plots to visualize the population changes over time. The ridgeline plots were composed of multiple nonparametric kernel density estimation (KDE) to estimate the probability density functions (PDF) of the peak amplitude component across the observation time at every min (Figure 3A). The higher peak amplitude population centered at around 0.25 nA could be seen slowly reducing over the course of 1 h, while lower peak amplitudes centered at around 0.15 nA started to emerge and became the major population after around 8 min. This observation agreed with the gel analysis on the digestion kinetics of the enzyme (Figure S10), indicating that the nanoconfinement of the SwaI within the nanopore and capillary did not alter its dsDNA cleavage activities.

To quantify the population differences over time, we utilized the fundamental properties of PDF (regardless of parametrically and nonparametrically derived PDF). The KDE estimates the PDF of the population distribution; the area under the curve (AUC) of the PDF must sum to 1 as all samples must fall within this PDF, and the probability of an event to be bound within this PDF is 100%. Subsequently, the AUC bound by two boundaries (Figure 3A) at the horizontal axis of the PDF will return the probability of the population, in this case, the probability of detecting a single molecule event with a current amplitude that falls within that AUC. Two boundaries (upper and lower) were defined by ±10% of the peak value of the RS-dsDNA population from the 1 min trace (Supporting Method for detailed explanations on the boundaries selection and probability calculation method); the 1 min trace was selected as for most samples the 1 min trace would contain both the RS-dsDNA and 1.5 kbp dsDNA populations. These boundaries were fixed and applied across all PDFs within the observation time, and the probabilities were calculated for each min. This analytical pipeline was used to quantify the variation of the dsDNA populations (3 kbp vs 1.5 kbp) over time. Figure 3B shows a scatter plot of the probability of detecting the RS-dsDNA translocation as a function of the digestion time. The probability dropped from close to 60% to around 15% after 30 min of digestion, reaching near 0% at around 40 min,

https://doi.org/10.1021/acsnano.4c15173
ACS Nano 2025, 19, 3839−3851

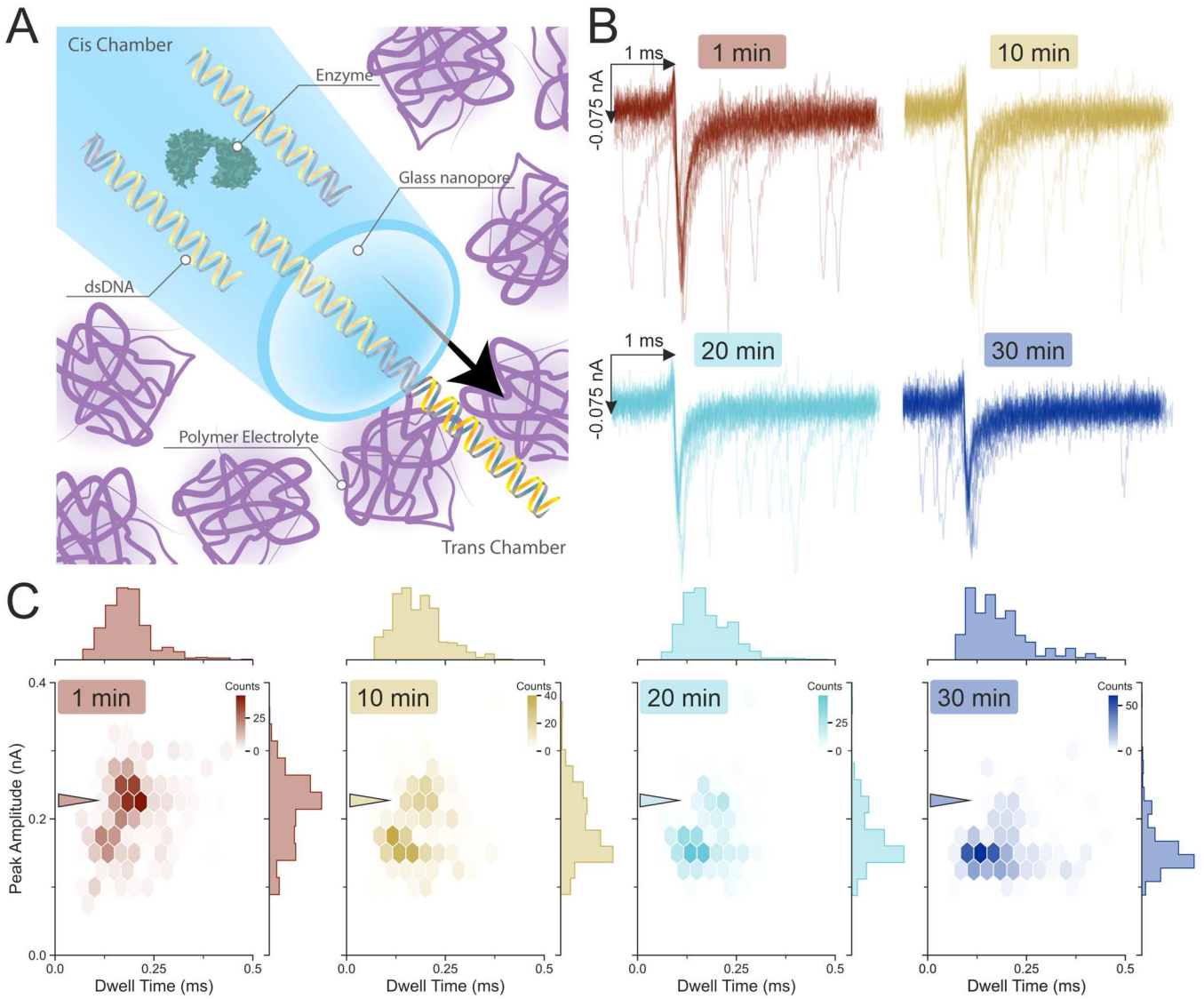

Figure 2. Restriction enzyme SwaI cleavage activities. (A) Schematic illustration of the glass nanopore detection setup. The cis chamber of the nanopore is filled with the restriction enzyme SwaI, the RS-dsDNA, the trans chamber is composed of a polymer electrolyte mixture (0.1 M KCl, 50% (w/v) PEG 35K). Application of a negative voltage causes the dsDNA to migrate from the cis to the trans chamber. The RS-dsDNA was mixed with the SwaI restriction enzyme and digestion buffer to a final concentration of 9.24 nM RS-dsDNA, 5 units of enzyme, and 1× digestion buffer. (B) 20 random translocation event peaks plotted as overlay. The cis chamber of the glass nanopore was filled with 10 nM RS-dsDNA diluted with buffer 3.1 (Table 1) containing 5 units of SwaI enzyme. (C) Population distribution of the translocation events at 1, 10, 20, and 30 min. The arrowheads across the four plots point at the population centered at approximately 0.2 ms and 0.25 nA. This population is attributed to the larger RS-dsDNA prior to digestion. As the time progresses to 10, 20 min and finally at 30 min, this population gradually disappears and a secondary population centered at approximately 0.15 ms and 0.15 nA begins to emerge; the side histograms of the peak amplitude axes show the emergence of the 0.15 nA population. The color bar represents the count of events found in each hexagon.

suggesting full digestion of the RS-dsDNA by SwaI. Additional SwaI concentrations ranging from 5 to 20 U were monitored, and their rates of the reactions were calculated through the same analytical pipeline as discussed in Figure 3A,B. Through plotting the rate of reaction against the SwaI concentration, our data showed that the SwaI's dsDNA cleavage activity is linearly proportional to the increasing concentration of SwaI (Figure 3C).

Effects of Salt on SwaI Cleavage Activity. The recommended buffer composition for SwaI (buffer 3.1) and its components is presented in Table 1. Alternative buffers can also be used (such as the buffer 4, buffer 2.1, and CutSmart); however, the activities of SwaI will be reduced, as mentioned by the supplier and also tested (Figure 4A,B). Buffer 2.1 and buffer 3.1 share similarities in the compositions of the buffer except that buffer 2.1 has lower NaCl concentration (50 mM NaCl) compared to buffer 3.1 (100 mM NaCl), while in buffer 4 and CutSmart, the NaCl is replaced with KOAc. These subtle differences in the composition of the buffer greatly affect the activity of SwaI.

Our nanopore setup was inert to buffer composition in the cis chamber.[37,40] This offered an opportunity for us to monitor the activities of SwaI under a slightly modified buffer composition in real time. We replaced the buffer in the final reaction mixture prior to loading into the glass nanopore and monitored the cleavage activity of the SwaI enzyme under

https://doi.org/10.1021/acsnano.4c15173
ACS Nano 2025, 19, 3839−3851

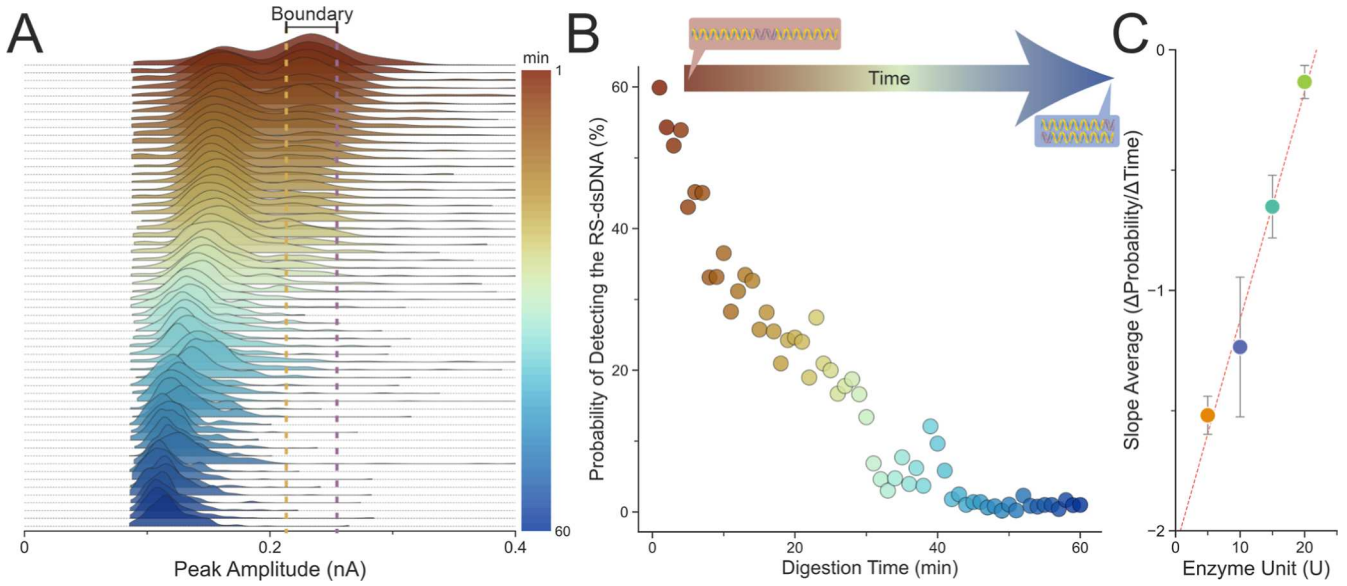

Figure 3. Digestion of RS-dsDNA monitored over the course of one hour. The RS-dsDNA was mixed with the SwaI restriction enzyme and digestion buffer to a final concentration of 9.24 nM RS-dsDNA, 5 units of enzyme, and 1× digestion buffer. (A) The ridgeline plot shows the gradual population changes from 1 to 60 min. (B) The probability of detecting the translocation of RS-dsDNA drops from 60% to near 0%. Two boundaries were defined as the ±10% of the peak value of the RS-dsDNA using the 1 min data, and the same boundaries were applied across all the data. The probability value was calculated by integrating the area under the curves (AUC) between the boundaries shown in (A); the initial starting percentage changes according to the width of the boundaries. (C) Enzyme reaction rate (slope average) plotted against the concentration of the enzyme. The enzyme reaction rate was calculated by fitting a linear regression line at the first 15 min (initial velocity region) of digestion under different enzyme concentrations (n = 3); the reaction rate obtained from the linear regression line is thus defined as the changes in probability of detecting the RS-dsDNA over the changes in time. The coefficient of determination for the fit is R^2 = 0.9822. Error bars represent standard error of the mean of the slope values between measurements. According to the manufacturer, a single unit of SwaI is defined as the amount of enzyme required to digest 1 μg of pXba DNA in 1 h at 25 °C in a total reaction volume of 50 μL.

different buffer conditions (Figure 4E). Two control experiments were also performed where one contained the RS-dsDNA without the addition of the SwaI enzyme (Figure S11) and the other where the RS-dsDNA were digested for 30 min before loading into the glass nanopore (Figure S12).

The probabilities of detecting the translocation of RS-dsDNA over 30 min of digestion time for different buffers are plotted in Figure 4C. The no enzyme controls showed consistently high probability (near 75%) of detecting the RS-dsDNA. The values did not change over time as indicated by the slope value of −0.03, indicating that, as expected, the materials inside the nanopore did not change. Similarly, the completely digested RS-dsDNA showed a low probability (near 12.5%) of detecting the RS-dsDNA, and this value did not change over the course of the digestion time (slope value = −0.03). When comparing the probabilities at 1 and 30 min, there were no significant differences (Figure 4D).

In agreement with the gel electrophoresis data (Figure 4A,B), the enzyme retained its activity in both buffer 3.1 and buffer 2.1. The probability of detecting the RS-dsDNA dropped to near 25% after 30 min from an initial value higher than 50%. Their slope values were −1.15 and −1.41, respectively, suggesting a rapid decline in the number of RS-dsDNA available in the buffer over a short period of time, as also evidenced by comparing the probabilities at 1 and 30 min (Figure 4D). Lastly, the digestion carried out with the nonideal buffers (buffer 4 and CutSmart), both produced small changes in the probabilities over time (slope value = −0.24 and −0.46 respectively), indicating that while the enzyme was not as active as in buffer 3.1 and buffer 2.1, it could still digest the RS-dsDNA, but at a slower rate. Statistical testing indicated a significant difference between 1 and 30 min for the CutSmart buffer, indicating that SwaI with the CutSmart buffer potentially operates at a slightly faster rate than in buffer 4. These observations overall agreed with the gel electrophoresis data, where both buffer 4 and CutSmart showed reduced activity when compared to buffer 3.1 and buffer 2.1 (Figure 4A).

Effects of RNA/DNA Mismatches on CRISPR-Cas9 Cleavage Activity. Part of the prokaryotic adaptive immunity mechanism used to cleave invading nucleic acids,[45] the CRISPR-Cas9 is a unique, RNA-guided endonuclease; its dsDNA cleavage activity relies on a Cas9 ribonucleoprotein (RNP) complex composed of a Cas9 protein, a tracrRNA, and a crRNA.[65−68] The Cas9 RNP scans the target dsDNA to look for a short trinucleotide site—a PAM site—and once a PAM site is identified, the target DNA sequence upstream of the PAM site is checked for complementarity against the crRNA. If complementary, a crRNA/DNA heteroduplex is formed and triggers the conformational activation of the Cas9 RNP's HNH endonuclease domain to cleave the target dsDNA strand 3−4 nucleotides upstream of the PAM sequence.[65−68] Notably, the Cas9 RNP does not dissociate from the DNA after cleavage[69] unlike restriction enzymes where they can proceed to cleave the next molecule of dsDNA.

The crRNA sequence can be designed to be complementary to different DNA sequences; targeting specific sequences in the genome enables the possibility of targeted gene editing. Thus, Cas9 is widely studied for its applications in genome engineering and therapeutic potential for correcting genetic disorders.[70] However, one challenge with using Cas9 RNP for genome editing is that it shows off-target activity. This happens

https://doi.org/10.1021/acsnano.4c15173
ACS Nano 2025, 19, 3839−3851

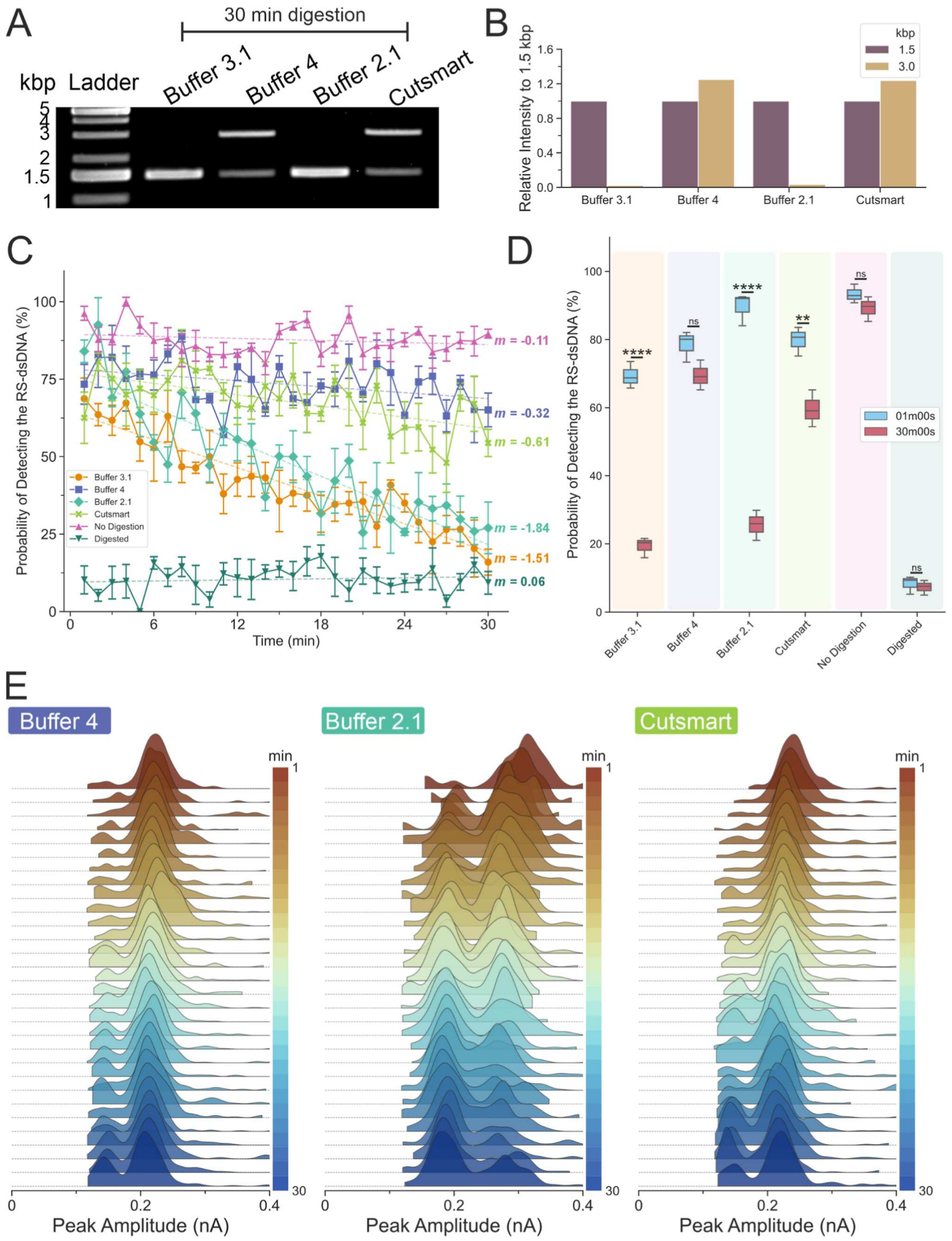

Figure 4. Buffer-dependent restriction enzyme kinetics. (A) Restriction digestion of the RS-dsDNA in different buffers. The optimal buffer for the restriction enzyme SwaI is the buffer 3.1, as recommended by the supplier. Three other buffers (4, 2.1 and CutSmart) were tested, and the activity of SwaI varied and resulted in lower digestion activity in buffer 4 and CutSmart. (B) The gel band intensity was quantified and calculated relative to the 1.5 kbp's band intensity within the sample lane (self-reference). (C) Probability of detecting 3 kbp dsDNA as a function of the digestion time for all the buffer tested and controls. *m* is the slope after fitting with the linear fit to the experimental data.

https://doi.org/10.1021/acsnano.4c15173
ACS Nano 2025, 19, 3839−3851

Figure 4. continued

Error bars are standard error of the mean. (D) Box plot comparing the probability of detecting the RS-dsDNA at 1 min and at 30 min. The two-tailed unpaired *t*-test was used to test the differences between the distribution of the probabilities to detect RS-dsDNA at 1 min and at 30 min. There are significant differences for buffer 3.1, buffer 2.1, and CutSmart at 1 min and at 30 min. The calculated values for buffer 3.1 at 1 min is 69.35 ± 3.94% and 19.28 ± 2.95% at 30 min, respectively; for buffer 4 at 1 min, it is 78.51 ± 4.55% and 69.43 ± 4.4%, respectively; for buffer 2.1 at 1 min, it is 89.54 ± 4.77% and 25.6 ± 4.44%, respectively; for CutSmart at 1 min, it is 79.81 ± 4.23% and 59.56 ± 5.42%, respectively; for no digestion at 1 min, it is 93.31 ± 2.76% and 89.17 ± 3.62%, respectively; for digested at 1 min, it is 8.52 ± 1.72% and 7.26 ± 2.15%, respectively. (ns, not significant; ****$P < 0.0001$; **$P < 0.005$; data assume normal distribution; Levene's test ($P > 0.05$) indicates data have homoscedasticity; $N = 3$). (E) Ridgeline plots for buffer 4, buffer 2.1, and CutSmart. The cis chamber of the glass nanopore was filled with 10 nM RS-dsDNA diluted with buffer 3.1, buffer 4, buffer 2.1, or CutSmart (Table 1) containing 5 units of SwaI enzyme.

when the crRNA is not fully complementary to the target DNA sequence but is still able to form a heteroduplex and triggers the HNH endonuclease domain.[71,72] Depending on the position of the mismatch between the crRNA and the target DNA sequence, the cleavage activity can be slower or abolished.[73−77]

The impacts of mismatches and off-target effects are critical problems to understand and address to unlock the potential of Cas9 for genome engineering and diagnostic application.[78,79] Traditional methods used to monitor the Cas9 RNP activity typically rely on sequencing[73,77] and electrophoresis,[74] which can be costly and slow and often lack real-time kinetic information. Solid-state nanopores have been used to study the binding affinities between the Cas9 RNP and the target dsDNA through the binding of catalytically inactive dCas9,[30−32] including studying the effects of mismatches on the binding of dCas9.[31] However, the high salt conditions used in these studies can interact with the dsDNA backbone,[55,80,81] leading to overwinding of the dsDNA.[82,83] The Cas9 RNP cleavage activity depends on unwinding the dsDNA duplex to form the heteroduplex and trigger the HNH endonuclease domain.[68,84,85] Thus, increasing overwinding of dsDNA at high salt conditions is associated with reduced activity of the Cas9 RNP.[84]

Our polymer electrolyte nanopore sensing system is ideal for rapidly studying the impact of mismatches on Cas9 RNP activity in real time in physiologically relevant conditions; we identified a PAM site near the SwaI restriction site of the RS-dsDNA and designed a crRNA sequence to target the DNA 30 bp downstream of the site. Similar to SwaI, the dsDNA cleavage by the Cas9 RNP caused the RS-dsDNA to be separated into two 1.5 kbp dsDNA (Figures 5A and S13). Additionally, we generated 4 off-target crRNA variants with mismatches at different positions (Figure 5B). The mismatches introduced are rU-dG, rG-dT, and rU-dC at position 1, 2, 3, or 4, upstream of the PAM site. The four off-target crRNA variants and the on-target crRNA were assembled into five different Cas9 RNPs, which were used to digest the RS-dsDNA. These were first assayed using traditional agarose gel electrophoresis with a single time point measurement after incubation at 25 °C (room temperature) for 30 min and then overnight at 4 °C (Figure 5C). Within 30 min of incubation at room temperature, the on-target crRNA led to the formation of the 1.5 kbp fragments. Similarly, the rG-dT variants at positions 2 and 3 upstream of PAM site also successfully cleaved into 1.5 kbp fragments. In contrast, the rU-dG variant at position 1 and rU-dC variant at position 4 resulted in incomplete digestions by 30 min. After overnight incubation of the mixture, additional 1.5 kbp dsDNA fragments were formed with the off-target 1 and 4 variants but the digestions were still incomplete.

We then used our polymer electrolyte nanopore sensor to monitor the Cas9 RNP's cleavage activity in real time at a physiologically relevant salt condition of 111 mM NaCl. We monitored the digestion of RS-dsDNA by different variants of the Cas9 RNPs over 30 min (Figure 6A). The off-target 1 and 4 variants showed little changes in the population of the 3.0 kbp dsDNA (peak amplitude of 0.3 nA). The off-target 2 and 3 variants showed a gradual reduction of 3.0 kbp population, indicating that the RS-dsDNA was getting digested inside the nanopore, despite the presence of the mismatches. However, this was occurring at a much slower rate than the on-target Cas9 RNP digestion. For the on-target digestion, most of the population that could be detected were 1.5 kbp fragments from the beginning of the experiment, indicating that the RS-dsDNA was nearly fully digested by the time the assay started. Indeed, studies[73,85] showed that on-target cleavage could cleave 80% of materials within 3 to 40 s and our method had a minimum delay of 60 s from mixing to measurement.

We quantified the probabilities of detecting the RS-dsDNA using all variants of crRNA-Cas9 RNP mixtures as well as the no digestion (Figure S14) and digested (Figure S15) (preincubated with on-target Cas9 RNP for 30 min prior to measurement) controls (Figure 6B). The no digestion and Cas9 RNP-digested controls showed that the probabilities to detect 3.0 kbp RS-dsDNA were near 90% and near 10%, respectively, throughout the experiment. The linear fitted slope had a minimum value of $m > -0.1$ over the measurement time and there was no significant difference found between these controls at 1 min and 30 min (Figure 6C). The off-target 1 and 4 variants showed a slow downward trend in the probability of detecting RS-dsDNA, with slope changes of $m < -0.1$ (Figure 6B). There were no significant differences in the probabilities of detecting RS-dsDNA between 1 and 30 min for these crRNA variants (Figure 6C), indicating a near negligible progression of the cleavage.

For the off-target 2 and 3 variants, the slopes were fitted to be $m < -1$, in sharp contrast to other variants and indicated faster cleavage activities (Figure 6B). Additionally, there were significant differences in the probabilities at 1 and 30 min where both variants showed lower probabilities of detecting the RS-dsDNA (Figure 6C). Overall, the two variants were more catalytically active and cleaved at a similar rate. The off-target 2 variant slowed the reaction rate significantly more than off-target 3 (Figure S16), despite the mutations being essentially the same sequence swap from rA-dT to rG-dT, and our study revealed that the position upstream of PAM played a significant role in determining the cleavage kinetics. Lastly, the on-target Cas9 RNPs cleaved the RS-dsDNA quite

https://doi.org/10.1021/acsnano.4c15173
ACS Nano 2025, 19, 3839−3851

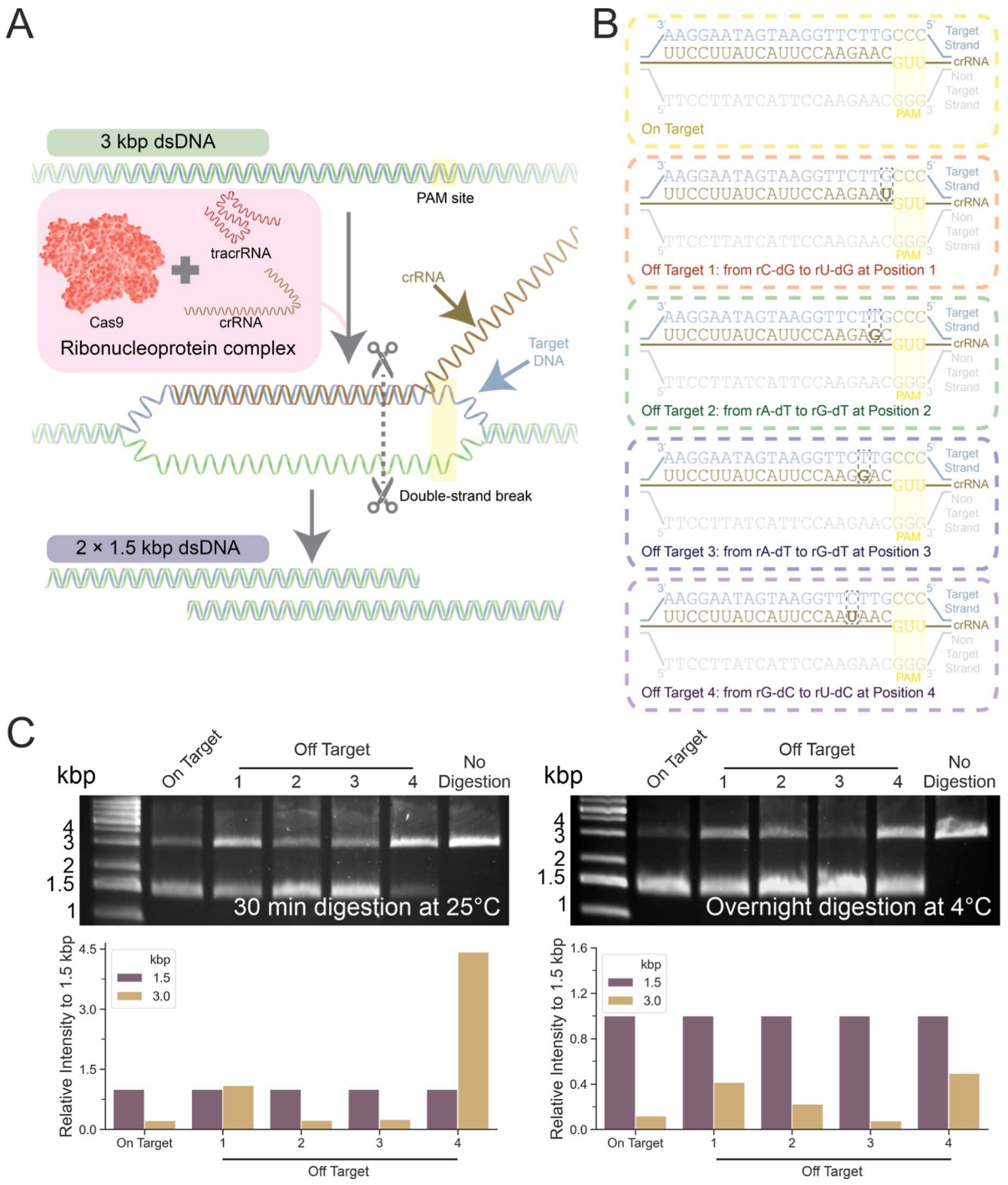

Figure 5. CRISPR-Cas9-mediated dsDNA cleavage. (A) Schematic illustrating the process of the Cas9 mediated cleavage on the 3 kbp RS-dsDNA. The Cas9 was mixed with tracrRNA and crRNA to form the RNP complex. The RNA guides the Cas9 RNP to the position next to the PAM site. The Cas9 RNP then carries out double stranded cleavage 3−4 bp upstream of the PAM site to cleave the dsDNA. This resulted in the formation of 2 × 1.5 kbp dsDNA. (B) On-target and off-target crRNA sequence. The full complementary sequence (On target) and the off target variations at different positions upstream of the PAM site and different mismatches. (C) Agarose gel electrophoresis following 30 min incubation at 25 °C and overnight incubation at 4 °C. Cas9 RNPs were formed with the on-target crRNA or off-target crRNA variants. The gel band intensity was quantified and calculated relative to the 1.5 kbp's band intensity within the sample lane (self-reference).

quickly such that there was only about a 25% probability of detecting the uncleaved RS-dsDNA by the time the experiment started. It then cleaved the remaining population at a slower rate with a slope of −0.8 throughout the remainder of the experiment.

Mismatches in the seed or PAM proximal region typically interrupt R-loop formation and often lead to higher dissociation rates of the Cas9 RNP from the target DNA sequence, reducing or eliminating cleavage activity as well.[31,74,77] Additionally, the cleavage activities could be lower due to distortions introducing steric hindrance between the HNH endonuclease domain and the heteroduplex. The variants we introduced form non-form noncanonical base pairing including wobble base pairing (rU-dG, rG-dT; position

https://doi.org/10.1021/acsnano.4c15173
ACS Nano 2025, 19, 3839−3851

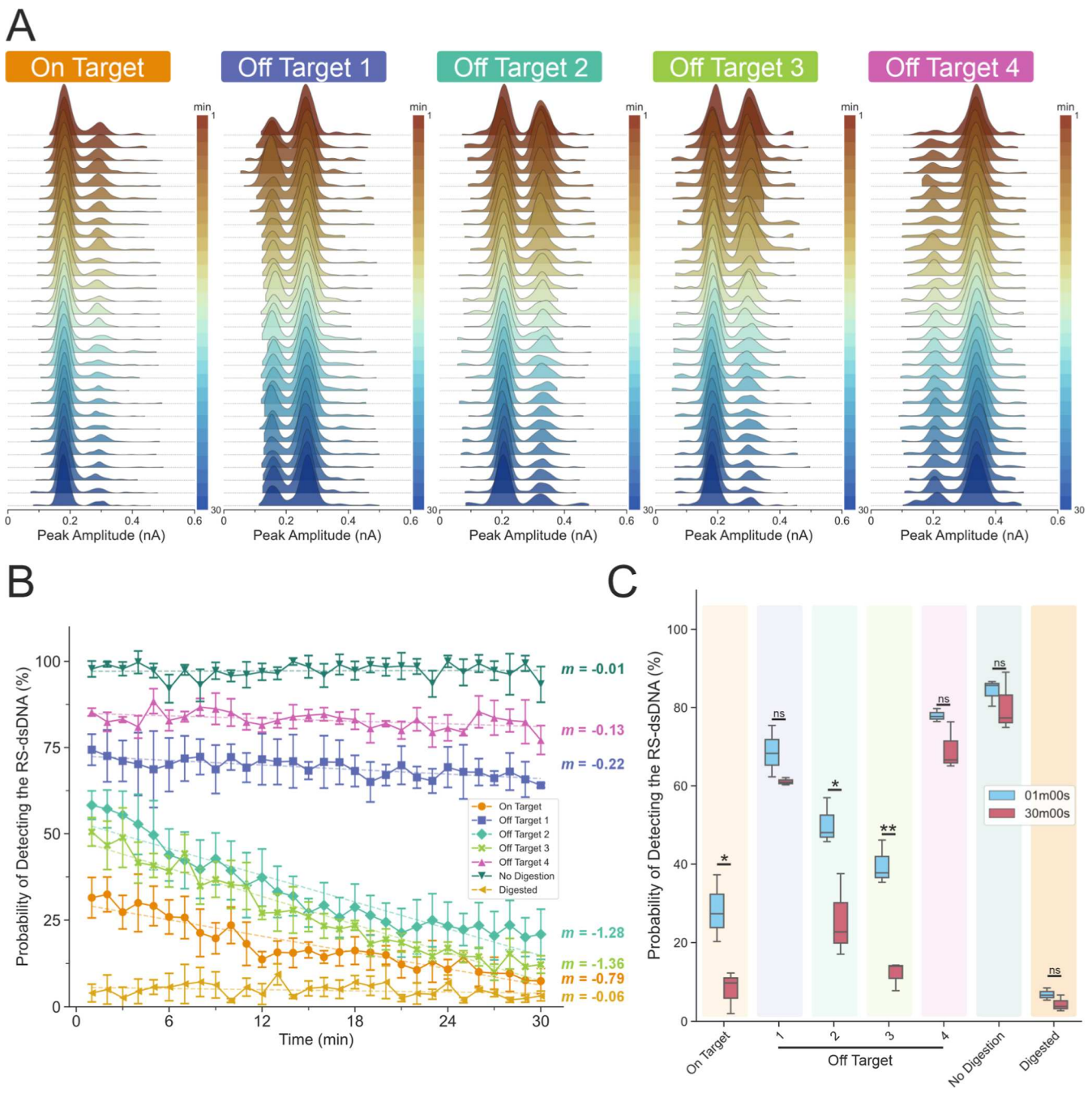

Figure 6. Measuring the activity of the Cas9 endonuclease with the nanopore. (A) Ridgeline plot showing the KDE estimated PDFs of the translocation experiment at each min for the 5 tested on-target and off-target crRNA sequences. (B) Probability of detecting 3 kbp dsDNA as a function of the digestion time for all the variants tested and controls. *m* is the slope after fitting with the linear fit to the experimental data. Error bars are standard error of the mean. (C) Box plot comparing the probability of detecting the RS-dsDNA at 1 min and at 30 min. The two-tailed unpaired *t*-test was used to test the differences between the distribution of the probabilities to detect RS-dsDNA at 1 min and at 30 min. There are significant differences for the on-target, off-target 2, and off-target 3 at 1 min and at 30 min. The calculated values for on target at 1 min are 28.31 ± 8.55% and 8.01 ± 5.37% at 30 min, respectively; for off target 1 at 1 min, it is 68.67 ± 6.57% and 61.08 ± 0.94%, respectively; for off-target 2 at 1 min, it is 50.25 ± 5.93% and 25.79 ± 10.6%, respectively; for off-target 3 at 1 min, it is 39.76 ± 5.65% and 12.04 ± 3.67%, respectively; for off-target 4 at 1 min, it is 77.95 ± 1.67% and 69.36 ± 6.11%, respectively; for no digestion at 1 min, it is 84.22 ± 3.38% and 80.44 ± 7.56%, respectively; for digested at 1 min, it is 8.52 ± 1.72% and 4.39 ± 2.07%, respectively. (ns, not significant; *$P < 0.05$; **$P < 0.005$; data assume normal distribution; Levene's test ($P > 0.05$) indicates data have homoscedasticity; $N = 3$, two-tailed *t*-test).

1−3)[86] and nonisosteric pyrimidine−pyrimidine base pairing (rU-dC, position 4)[87] when constrained within the Cas9 RNPs complexes.[74] In our experiments, mismatches in the seed region at positions 1 and 4 lead to suppressed cleavage; however, we have observed off-target or mismatch tolerance at positions 2 and 3 that result in cleavage kinetics that are slightly slower but comparable to the on-target Cas9 RNP. Non-canonical binding (wobble base pairing) may contribute to stabilizing the binding in these cases. At position 1, there is also a potential wobble base pairing (rU-dG). However, due to

https://doi.org/10.1021/acsnano.4c15173
ACS Nano 2025, 19, 3839−3851

the position of the mismatch, the sequence rigidity is expected to hinder the binding of the wobble base pair, which could contribute to the suppression of the cleavage activity due to steric hindrance.[31,74,77] These measurements demonstrate the potential of our nanopore sensor to rapidly provide detailed kinetic information on the activity of enzymes under physiological conditions.

CONCLUSIONS

In this study, we developed and validated a solid-state nanopore-based kinetic sensing system to monitor the activities of endonucleases such as the restriction enzyme, SwaI, and CRISPR-Cas9 ribonucleoprotein endonuclease in physiologically relevant salt conditions. Our nanopore sensor effectively distinguishes between the reactant (RS-dsDNA) and cleavage products (1.5 kbp dsDNA) due to the molecular weight differences and thus is able to quantify the population with single molecule resolution. As the digestion progressed, the population differences were monitored in real time, and an observable depletion of the RS-dsDNA could be seen for both the restriction enzyme and CRISPR-Cas9 ribonucleoprotein endonuclease.

We have presented a proof of concept for a single molecule sensing system that enables real-time label-free measurements of enzyme activity. Several improvements to the measurement and analysis system would allow us to further expand our applications. For example, the hardware could be improved by implementing a temperature controlling unit to allow us to monitor temperature-sensitive endonucleases. This improvement could also allow us to dynamically control the temperature of the electrolyte bath to enhance, reduce, or abolish the endonuclease activity. Second, it is hard to perform liquid exchange or mixing after backfilling the current glass capillaries. To this end, a wider outer diameter quartz capillaries tube could be used to fabricate the nanopores to facilitate solution mixing in the future. Third, the boundary selection for the quantification of the probability was fixed and applied across all the PDFs. However, to allow for a longer experiment, the boundary selection and calculation for the data analysis could dynamically be adapted to the baseline current level.

Unlike most solid-state nanopore approaches, the method developed here takes advantage of the unique properties of the polymer electrolyte bath measurement system to eliminate the need for high concentrations of salt to improve the signal-to-noise ratio,[37,40] thus allowing us to monitor the activities of the restriction enzyme and CRISPR-Cas9 ribonucleoprotein endonuclease at physiological salt conditions. Since the magnitude of the signal does not depend on the properties of the buffer, as we previously demonstrated,[37] salt-sensitive analytes such as intrinsically disordered proteins[88,89] can be analyzed and monitored over time at single molecule resolution with the nanopore. For example, the aggregation of amyloid materials[41,90] under different salt conditions can be monitored as aggregation propensity is different under different ionic strengths.[91−96] While the method developed here focuses on monitoring the transition of reactant to product, the same method can, in principle, be applied to study other reactions such as full digestion of materials (such as full or partial digestion of nucleic acid by DNase)[97] and the emergence of larger biomolecules during overtime (such as protein aggregation).[91−96]

METHODS

Solid-State Nanopore Fabrication and Measurement. The glass solid-state nanopore (nanopipette) was fabricated by a SU-P2000 laser puller (World Precision Instruments). Quartz capillaries of 1.0 mm outer diameter and 0.5 mm inner diameter with filament (QF100-50-7.5; Sutter Instrument) were used for nanopore fabrication. A two-line protocol was used: line 1, HEAT 750/FIL 4/VEL 30/DEL 150/PUL 80, followed by line 2, HEAT 725/FIL 3/VEL 40/DEL 135/PUL 180. The pulling protocol is instrument specific, and there is variation between pullers. The nanopore dimension was confirmed by scanning electron microscopy.

The analyte-filled nanopore was fitted with a Ag/AgCl working electrode and immersed in the polymer electrolyte bath with a Ag/AgCl reference electrode. Ionic current trace was recorded by using the MultiClamp 700B patch-clamp amplifier (Molecular Devices) in voltage-clamp mode. The sampling bandwidth was approximately 52 kHz. The signal was filtered using a low-pass filter at 20 kHz setting and digitized with a Digidata 1550B (Molecular Devices) at a 100 kHz (10 μs) sampling rate. The software used for recording was a pClamp 10 (Molecular Devices). For translocation events analysis, the threshold level was defined at least 10 sigma away from the baseline, and only events that were above this threshold would be identified as the translocation of the molecule. The analysis script can be accessed here: https://github.com/chalmers4c/Nanopore_event_detection.

Polymer Electrolyte Bath Generation. To generate 10 mL of the 50% (w/v) PEG 35K KCl electrolyte bath, 5 g of PEG 35K (94646; Sigma-Aldrich) was mixed with 1 mL of 1 M KCl (A11662.0B; Thermo Fisher) and 4 mL of ddH_2O. The mixture was then incubated inside an 85 °C oven for 2 h followed by overnight incubation at 37 °C. All the electrolyte baths were stored at room temperature inside a box protected from sunlight. All the electrolyte baths were discarded one month after generation.

Kinetic Translocation Experiment. Prior to the measurement, the RS-dsDNA, the restriction enzyme SwaI with the restriction digestion buffer was mixed so that the RS-dsDNA, SwaI, and the buffer were at 10 nM, 5 units, and 1×, respectively. The mixture was immediately loaded into the glass nanopore and immersed into the polymer electrolyte bath with a Ag/AgCl working electrode fitted into the nanopore. From mixing the reactants to the start of measurement, we estimated a delay of 1 min. We applied a waveform composed of 3.5 s of +100 mV followed by 6 s of −700 mV. The single molecule events recorded between 4 and 9 s of each trace were used for all analysis. The Supporting Information contains more details on the method for the analysis of the trace. A custom written python script was used for the calculation of the boundaries and the AUC and can be accessed here: https://github.com/chalmers4c/KDE_AUC-calculation/

The fitting was carried out with python, and the linear fit was calculated by the sum of least-squares method.

CRISPR-Cas9 Ribonucleoproteins Complex Assembly and Reaction. The recombinant *S. pyogenes* Cas9 was used (1081058; IDTDNA) throughout the study. The tracrRNA (1072532; IDTDNA) and crRNA were synthesized and provided by IDTDNA. The tracrRNA and crRNA were mixed and diluted with the duplex buffer (30 mM HEPES, pH 7.5; 100 mM potassium acetate; 11-01-03-01; IDTDNA). The final mixture contained 40 μM of tracrRNA and 40 μM of crRNA. The mixture was incubated at 95 °C for 5 min and then at 25 °C until use. To assemble the Cas9 RNPs, the RNA mixture after the incubation was mixed with the Cas9 proteins and diluted with the digestion buffer (111 mM HEPES at pH 8.0, 6 mM $MgCl_2$, 111 mM NaCl), so that the final mixture contained 40 μM tracrRNA, 40 μM of crRNA and 18.6 μM of Cas9 proteins, followed by incubation at 25 °C for 30 min, and stored at 4 °C until use. For longer storage, the Cas9 RNPs were snap frozen with liquid nitrogen and stored at −80 °C. For the kinetic translocation experiment, the Cas9 RNPs were mixed with RS-dsDNA to a final concentration of 1000 nM Cas9 RNPs and 10 nM dsDNA (100:1 Cas9 RNP to dsDNA ratio) and loaded into the nanopore immediately prior to use.

https://doi.org/10.1021/acsnano.4c15173
ACS Nano 2025, 19, 3839−3851

The measurement setups and routines were the same as the kinetic translocation experiment session.

ASSOCIATED CONTENT

Data Availability Statement

All the translocation trace data supporting this work can be freely accessed via the University of Leeds data repository: 10.5518/1454

Supporting Information

The Supporting Information is available free of charge at https://pubs.acs.org/doi/10.1021/acsnano.4c15173.

Supporting note on polymer electrolyte-modified solid-state nanopore mechanism, generation of the RS-dsDNA and the sequence data, generation of the RS-dsDNA, restriction digestion of the RS-dsDNA, Cas9-related crRNA sequence and digestion, KDE and probability calculations, and relevant supporting figures (PDF)

AUTHOR INFORMATION

Corresponding Author

Chalmers C. C. Chau − *Bragg Centre for Materials Research, School of Electronic and Electrical Engineering, University of Leeds, Leeds LS2 9JT, U.K.;* orcid.org/0000-0002-3134-6798; Email: c.c.chau@leeds.ac.uk

Authors

Nicole E. Weckman − *Institute for Studies in Transdisciplinary Engineering Education & Practice, Department of Chemical Engineering & Applied Chemistry, University of Toronto, Toronto M5S 1A4, Canada;* orcid.org/0000-0001-5894-4926

Emma E. Thomson − *School of Bioscience, University of Sheffield, Sheffield S10 2TN, U.K.*

Paolo Actis − *Bragg Centre for Materials Research, School of Electronic and Electrical Engineering, University of Leeds, Leeds LS2 9JT, U.K.;* orcid.org/0000-0002-7146-1854

Complete contact information is available at: https://pubs.acs.org/10.1021/acsnano.4c15173

Author Contributions

C.C.C.C. designed and performed all experiments. C.C.C.C. analyzed all data. C.C.C.C. illustrated all schematics. N.E.W., E.E.T., and P.A. provided the concept of Cas9 detection and helped with data analysis. P.A. helped with data analysis and acquired the funding. All authors wrote and corrected the manuscript.

Funding

C.C.C.C. and P.A acknowledge funding from the Engineering and Physical Sciences Research Council UK (EPSRC) Healthcare Technologies for the grant EP/W004933/1 and C.C.C.C., P.A. and E.E.T. acknowledge the Biotechnology and Biological Sciences Research Council (BBSRC) for the grant BB/X003086/1. For the purpose of Open Access, the authors have applied a CC BY public copyright license to any Author Accepted Manuscript version arising from this submission.

Notes

The authors declare no competing financial interest.

The preprint version of this work can be found in bioRxiv.[98]

ACKNOWLEDGMENTS

We thank the group of bioelectronics member and Professor Christoph Wälti of University of Leeds for providing insightful feedback. We thank Dr Alexander Kulak of University of Leeds for imaging the nanopore with the scanning electron microscopy. C.C.C.C. acknowledges the scientific contributions of Dame Jocelyn Bell Burnell, particularly her discovery of the "PSR B1919 + 21 (CP 1919)" pulsar, and the iconic design of Joy Division's "Unknown Pleasures" album cover, both of which inspired the creation of the plots in Figures 3, 4, and 6, and the table of content graphic.

ABBREVIATIONS

AUC	area under the curve
KDE	kernel density estimation
PEG	poly(ethylene) glycol
PCR	polymerase chain reaction
RS-dsDNA	restriction site containing dsDNA
CRISPR	clustered regularly interspaced short palindromic repeats
PAM	protospacer adjacent motif
RNP	ribonucleoprotein

REFERENCES

(1) Miller, H.; Zhou, Z.; Shepherd, J.; Wollman, A. J. M.; Leake, M. C. Single-molecule techniques in biophysics: a review of the progress in methods and applications. *Rep. Prog. Phys.* **2018**, *81*, 024601.

(2) Banerjee, S.; et al. Cutting-Edge Single-Molecule Technologies Unveil New Mechanics in Cellular Biochemistry. *Annu. Rev. Biophys.* **2021**, *50*, 419−445.

(3) Xu, X.; et al. The New Era of High-Throughput Nanoelectrochemistry. *Anal. Chem.* **2023**, *95*, 319−356.

(4) Müller, D. J.; et al. Atomic Force Microscopy-Based Force Spectroscopy and Multiparametric Imaging of Biomolecular and Cellular Systems. *Chem. Rev.* **2021**, *121*, 11701−11725.

(5) Möckl, L.; Moerner, W. E. Super-resolution Microscopy with Single Molecules in Biology and Beyond−Essentials, Current Trends, and Future Challenges. *J. Am. Chem. Soc.* **2020**, *142*, 17828−17844.

(6) Bustamante, C. J.; Chemla, Y. R.; Liu, S.; Wang, M. D. Optical tweezers in single-molecule biophysics. *Nat. Rev. Methods Primers* **2021**, *1*, 25.

(7) Bacic, L.; Sabantsev, A.; Deindl, S. Recent advances in single-molecule fluorescence microscopy render structural biology dynamic. *Curr. Opin. Struct. Biol.* **2020**, *65*, 61−68.

(8) Ying, Y.-L.; et al. Single-entity electrochemistry at confined sensing interfaces. *Sci. China:Chem.* **2020**, *63*, 589−618.

(9) Ahmed, S. A.; et al. Iontronic Sensing Based on Confined Ion Transport. *Anal. Chem.* **2024**, *96*, 8056−8077.

(10) Wang, Y.; Zhao, Y.; Bollas, A.; Wang, Y.; Au, K. F. Nanopore sequencing technology, bioinformatics and applications. *Nat. Biotechnol.* **2021**, *39*, 1348−1365.

(11) Xue, L.; et al. Solid-state nanopore sensors. *Nat. Rev. Mater.* **2020**, *5*, 931−951.

(12) Albrecht, T. Single-Molecule Analysis with Solid-State Nanopores. *Annu. Rev. Anal. Chem.* **2019**, *12*, 371−387.

(13) Mayer, S. F.; Cao, C.; Dal Peraro, M. Biological nanopores for single-molecule sensing. *iScience* **2022**, *25*, 104145.

(14) Ying, Y.-L.; et al. Nanopore-based technologies beyond DNA sequencing. *Nat. Nanotechnol.* **2022**, *17*, 1136−1146.

(15) Varongchayakul, N.; Song, J.; Meller, A.; Grinstaff, M. W. Single-molecule protein sensing in a nanopore: a tutorial. *Chem. Soc. Rev.* **2018**, *47*, 8512−8524.

(16) Platnich, C. M.; Earle, M. K.; Keyser, U. F. Chemical Annealing Restructures RNA for Nanopore Detection. *J. Am. Chem. Soc.* **2024**, *146*, 12919−12924.

(17) Bandara, Y. M. N. D. Y.; Farajpour, N.; Freedman, K. J. Nanopore Current Enhancements Lack Protein Charge Dependence and Elucidate Maximum Unfolding at Protein's Isoelectric Point. *J. Am. Chem. Soc.* **2022**, *144*, 3063−3073.

(18) Gao, T.; et al. Label-Free Resistance Cytometry at the Orifice of a Nanopipette. *Anal. Chem.* **2021**, *93*, 2942−2949.
(19) Shumyantseva, V. V.; et al. Enzymology on an Electrode and in a Nanopore: Analysis Algorithms, Enzyme Kinetics, and Perspectives. *Bionanosci.* **2022**, *12*, 1341−1355.
(20) Willems, K.; Van Meervelt, V.; Wloka, C.; Maglia, G. Single-molecule nanopore enzymology. *Philos. Trans. R. Soc., B* **2017**, *372*, 20160230.
(21) Sheng, Y.; Zhang, S.; Liu, L.; Wu, H. C. Measuring Enzymatic Activities with Nanopores. *ChemBioChem* **2020**, *21*, 2089−2097.
(22) Wloka, C.; et al. Label-Free and Real-Time Detection of Protein Ubiquitination with a Biological Nanopore. *ACS Nano* **2017**, *11*, 4387−4394.
(23) Galenkamp, N. S.; Biesemans, A.; Maglia, G. Directional conformer exchange in dihydrofolate reductase revealed by single-molecule nanopore recordings. *Nat. Chem.* **2020**, *12*, 481−488.
(24) Robinson, P. K. Enzymes: principles and biotechnological applications. *Essays Biochem.* **2015**, *59*, 1−41.
(25) Cheley, S.; Xie, H.; Bayley, H. A Genetically Encoded Pore for the Stochastic Detection of a Protein Kinase. *ChemBioChem* **2006**, *7*, 1923−1927.
(26) Harrington, L.; Cheley, S.; Alexander, L. T.; Knapp, S.; Bayley, H. Stochastic detection of Pim protein kinases reveals electrostatically enhanced association of a peptide substrate. *Proc. Natl. Acad. Sci. U.S.A.* **2013**, *110*, E4417−E4426.
(27) Harrington, L.; Alexander, L. T.; Knapp, S.; Bayley, H. Single-Molecule Protein Phosphorylation and Dephosphorylation by Nanopore Enzymology. *ACS Nano* **2019**, *13*, 633−641.
(28) Harrington, L.; Alexander, L. T.; Knapp, S.; Bayley, H. Pim Kinase Inhibitors Evaluated with a Single-Molecule Engineered Nanopore Sensor. *Angew. Chem., Int. Ed.* **2015**, *54*, 8154−8159.
(29) Nouri, R.; Jiang, Y.; Lian, X. L.; Guan, W. Sequence-Specific Recognition of HIV-1 DNA with Solid-State CRISPR-Cas12a-Assisted Nanopores (SCAN). *ACS Sensors* **2020**, *5*, 1273−1280.
(30) Weckman, N. E.; et al. Multiplexed DNA Identification Using Site Specific dCas9 Barcodes and Nanopore Sensing. *ACS Sensors* **2019**, *4*, 2065−2072.
(31) Sandler, S. E.; et al. Sensing the DNA-mismatch tolerance of catalytically inactive Cas9 via barcoded DNA nanostructures in solid-state nanopores. *Nat. Biomed. Eng.* **2024**, *8*, 325−334.
(32) Yang, W.; et al. Detection of CRISPR-dCas9 on DNA with Solid-State Nanopores. *Nano Lett.* **2018**, *18*, 6469−6474.
(33) Ma, H.; Wang, Y.; Li, Y. X.; Xie, B. K.; Hu, Z. L.; Yu, R. J.; Long, Y. T.; Ying, Y. L. Label-Free Mapping of Multivalent Binding Pathways with Ligand−Receptor-Anchored Nanopores. *J. Am. Chem. Soc.* **2024**, *146*, 28014−28022.
(34) Kowalczyk, S. W.; Wells, D. B.; Aksimentiev, A.; Dekker, C. Slowing down DNA Translocation through a Nanopore in Lithium Chloride. *Nano Lett.* **2012**, *12*, 1038−1044.
(35) Plesa, C.; et al. Fast Translocation of Proteins through Solid State Nanopores. *Nano Lett.* **2013**, *13*, 658−663.
(36) Chau, C. C.; Radford, S. E.; Hewitt, E. W.; Actis, P. Macromolecular Crowding Enhances the Detection of DNA and Proteins by a Solid-State Nanopore. *Nano Lett.* **2020**, *20*, 5553−5561.
(37) Chau, C.; et al. Probing RNA Conformations Using a Polymer−Electrolyte Solid-State Nanopore. *ACS Nano* **2022**, *16*, 20075−20085.
(38) Confederat, S.; Sandei, I.; Mohanan, G.; Wälti, C.; Actis, P. Nanopore fingerprinting of supramolecular DNA nanostructures. *Biophys. J.* **2022**, *121*, 4882−4891.
(39) Confederat, S.; Lee, S.; Vang, D.; Soulias, D.; Marcuccio, F.; Peace, T. I.; Edwards, M. A.; Strobbia, P.; Samanta, D.; Wälti, C.; et al. Next-Generation Nanopore Sensors Based on Conductive Pulse Sensing for Enhanced Detection of Nanoparticles. *Small* **2024**, *20*, 2305186.
(40) Marcuccio, F.; et al. Mechanistic Study of the Conductance and Enhanced Single-Molecule Detection in a Polymer−Electrolyte Nanopore. *ACS Nanosci. Au* **2023**, *3*, 172−181.
(41) Meyer, N.; Janot, J.-M.; Torrent, J.; Balme, S. Real-Time Fast Amyloid Seeding and Translocation of α-Synuclein with a Nanopipette. *ACS Cent. Sci.* **2022**, *8*, 441−448.
(42) Meyer, N.; Arroyo, N.; Roustan, L.; Janot, J.; Charles-Achille, S.; Torrent, J.; Picaud, F.; Balme, S. Secondary Nucleation of Aβ Revealed by Single-Molecule and Computational Approaches. *Advanced Science* **2024**, *11*, 2404916.
(43) Sandler, S. E.; et al. Multiplexed Digital Characterization of Misfolded Protein Oligomers via Solid-State Nanopores. *J. Am. Chem. Soc.* **2023**, *145*, 25776−25788.
(44) Shen, B. W.; Heiter, D. F.; Lunnen, K. D.; Wilson, G. G.; Stoddard, B. L. DNA recognition by the SwaI restriction endonuclease involves unusual distortion of an 8 base pair A:T-rich target. *Nucleic Acids Res.* **2017**, *45*, 1516−1528.
(45) Barrangou, R.; et al. CRISPR Provides Acquired Resistance Against Viruses in Prokaryotes. *Science* **2007**, *315*, 1709−1712.
(46) Wanunu, M.; Sutin, J.; McNally, B.; Chow, A.; Meller, A. DNA Translocation Governed by Interactions with Solid-State Nanopores. *Biophys. J.* **2008**, *95*, 4716−4725.
(47) Li, J.; Talaga, D. S. The distribution of DNA translocation times in solid-state nanopores. *J. Phys.: Condens. Matter* **2010**, *22*, 454129.
(48) Kesselheim, S.; Müller, W.; Holm, C. Origin of Current Blockades in Nanopore Translocation Experiments. *Phys. Rev. Lett.* **2014**, *112*, 018101.
(49) Gibson, D. G.; et al. Enzymatic assembly of DNA molecules up to several hundred kilobases. *Nat. Methods* **2009**, *6*, 343−345.
(50) Li, Y.; Sandler, S. E.; Keyser, U. F.; Zhu, J. DNA Volume, Topology, and Flexibility Dictate Nanopore Current Signals. *Nano Lett.* **2023**, *23*, 7054−7061.
(51) Cadinu, P.; Kang, M.; Nadappuram, B. P.; Ivanov, A. P.; Edel, J. B. Individually Addressable Multi-nanopores for Single-Molecule Targeted Operations. *Nano Lett.* **2020**, *20*, 2012−2019.
(52) Cadinu, P.; et al. Double Barrel Nanopores as a New Tool for Controlling Single-Molecule Transport. *Nano Lett.* **2018**, *18*, 2738−2745.
(53) Cadinu, P.; et al. Single Molecule Trapping and Sensing Using Dual Nanopores Separated by a Zeptoliter Nanobridge. *Nano Lett.* **2017**, *17*, 6376−6384.
(54) Steinbock, L. J.; Otto, O.; Chimerel, C.; Gornall, J.; Keyser, U. F. Detecting DNA Folding with Nanocapillaries. *Nano Lett.* **2010**, *10*, 2493−2497.
(55) Smeets, R. M. M.; et al. Salt Dependence of Ion Transport and DNA Translocation through Solid-State Nanopores. *Nano Lett.* **2006**, *6*, 89−95.
(56) Bošković, F.; Zhu, J.; Chen, K.; Keyser, U. F. Monitoring G-Quadruplex Formation with DNA Carriers and Solid-State Nanopores. *Nano Lett.* **2019**, *19*, 7996−8001.
(57) Lastra, L. S.; Bandara, Y. M. N. D. Y.; Sharma, V.; Freedman, K. J. Protein and DNA Yield Current Enhancements, Slow Translocations, and an Enhanced Signal-to-Noise Ratio under a Salt Imbalance. *ACS Sensors* **2022**, *7*, 1883−1893.
(58) Charron, M.; Briggs, K.; King, S.; Waugh, M.; Tabard-Cossa, V. Precise DNA Concentration Measurements with Nanopores by Controlled Counting. *Anal. Chem.* **2019**, *91*, 12228−12237.
(59) Karau, P.; Tabard-Cossa, V. Capture and Translocation Characteristics of Short Branched DNA Labels in Solid-State Nanopores. *ACS Sensors* **2018**, *3*, 1308−1315.
(60) Kong, J.; Bell, N. A. W.; Keyser, U. F. Quantifying Nanomolar Protein Concentrations Using Designed DNA Carriers and Solid-State Nanopores. *Nano Lett.* **2016**, *16*, 3557−3562.
(61) Chen, K.; et al. Ionic Current-Based Mapping of Short Sequence Motifs in Single DNA Molecules Using Solid-State Nanopores. *Nano Lett.* **2017**, *17*, 5199−5205.
(62) Wang, V.; Ermann, N.; Keyser, U. F. Current Enhancement in Solid-State Nanopores Depends on Three-Dimensional DNA Structure. *Nano Lett.* **2019**, *19*, 5661−5666.

https://doi.org/10.1021/acsnano.4c15173
ACS Nano 2025, 19, 3839−3851

(63) Lastra, L. S.; Bandara, Y. M. N. D. Y.; Nguyen, M.; Farajpour, N.; Freedman, K. J. On the origins of conductive pulse sensing inside a nanopore. *Nat. Commun.* **2022**, *13*, 2186.
(64) Ivanov, A. P.; et al. On-Demand Delivery of Single DNA Molecules Using Nanopipets. *ACS Nano* **2015**, *9*, 3587−3595.
(65) Bhattacharya, S.; Satpati, P. Insights into the Mechanism of CRISPR/Cas9-Based Genome Editing from Molecular Dynamics Simulations. *ACS Omega* **2023**, *8*, 1817−1837.
(66) Pickar-Oliver, A.; Gersbach, C. A. The next generation of CRISPR−Cas technologies and applications. *Nat. Rev. Mol. Cell Biol.* **2019**, *20*, 490−507.
(67) Wiedenheft, B.; et al. RNA-guided complex from a bacterial immune system enhances target recognition through seed sequence interactions. *Proc. Natl. Acad. Sci. U.S.A.* **2011**, *108*, 10092−10097.
(68) Pacesa, M.; et al. R-loop formation and conformational activation mechanisms of Cas9. *Nature* **2022**, *609*, 191−196.
(69) Sternberg, S. H.; Redding, S.; Jinek, M.; Greene, E. C.; Doudna, J. A. DNA interrogation by the CRISPR RNA-guided endonuclease Cas9. *Nature* **2014**, *507*, 62−67.
(70) Li, T.; Yang, Y.; Qi, H.; Cui, W.; Zhang, L.; Fu, X.; He, X.; Liu, M.; Li, P. f.; Yu, T. CRISPR/Cas9 therapeutics: progress and prospects. *Signal Transduction Targeted Ther.* **2023**, *8*, 36.
(71) Cameron, P.; et al. Mapping the genomic landscape of CRISPR−Cas9 cleavage. *Nat. Methods* **2017**, *14*, 600−606.
(72) Tsai, S. Q.; et al. CIRCLE-seq: a highly sensitive in vitro screen for genome-wide CRISPR−Cas9 nuclease off-targets. *Nat. Methods* **2017**, *14*, 607−614.
(73) Zhang, L.; et al. Systematic in vitro profiling of off-target affinity, cleavage and efficiency for CRISPR enzymes. *Nucleic Acids Res.* **2020**, *48*, 5037−5053.
(74) Pacesa, M.; et al. Structural basis for Cas9 off-target activity. *Cell* **2022**, *185*, 4067.
(75) Boyle, E. A.; Becker, W. R.; Bai, H. B.; Chen, J. S.; Doudna, J. A.; Greenleaf, W. J. Quantification of Cas9 binding and cleavage across diverse guide sequences maps landscapes of target engagement. *Sci. Adv.* **2021**, *7*, No. eabe5496.
(76) Ivanov, I. E.; et al. Cas9 interrogates DNA in discrete steps modulated by mismatches and supercoiling. *Proc. Natl. Acad. Sci. U.S.A.* **2020**, *117*, 5853−5860.
(77) Jones, S. K.; et al. Massively parallel kinetic profiling of natural and engineered CRISPR nucleases. *Nat. Biotechnol.* **2021**, *39*, 84−93.
(78) Samanta, D.; Ebrahimi, S. B.; Ramani, N.; Mirkin, C. A. Enhancing CRISPR-Cas-Mediated Detection of Nucleic Acid and Non-nucleic Acid Targets Using Enzyme-Labeled Reporters. *J. Am. Chem. Soc.* **2022**, *144*, 16310−16315.
(79) Kong, D.; et al. Direct SARS-CoV-2 Nucleic Acid Detection by Y-Shaped DNA Dual-Probe Transistor Assay. *J. Am. Chem. Soc.* **2021**, *143*, 17004−17014.
(80) Gebala, M.; et al. Cation−Anion Interactions within the Nucleic Acid Ion Atmosphere Revealed by Ion Counting. *J. Am. Chem. Soc.* **2015**, *137*, 14705−14715.
(81) Gebala, M.; Bonilla, S.; Bisaria, N.; Herschlag, D. Does Cation Size Affect Occupancy and Electrostatic Screening of the Nucleic Acid Ion Atmosphere? *J. Am. Chem. Soc.* **2016**, *138*, 10925−10934.
(82) Cruz-León, S.; et al. Twisting DNA by salt. *Nucleic Acids Res.* **2022**, *50*, 5726−5738.
(83) SantaLucia, J. A unified view of polymer, dumbbell, and oligonucleotide DNA nearest-neighbor thermodynamics. *Proc. Natl. Acad. Sci. U.S.A.* **1998**, *95*, 1460−1465.
(84) Li, Y.; et al. CRISPR-Cas9 Activities with Truncated 16-Nucleotide RNA Guides Are Tuned by Target Duplex Stability Beyond the RNA/DNA Hybrid. *Biochemistry* **2023**, *62*, 2541−2548.
(85) Gong, S.; Yu, H. H.; Johnson, K. A.; Taylor, D. W. DNA Unwinding Is the Primary Determinant of CRISPR-Cas9 Activity. *Cell Rep.* **2018**, *22*, 359−371.
(86) Kimsey, I. J.; Petzold, K.; Sathyamoorthy, B.; Stein, Z. W.; Al-Hashimi, H. M. Visualizing transient Watson−Crick-like mispairs in DNA and RNA duplexes. *Nature* **2015**, *519*, 315−320.
(87) Leontis, N. B. The non-Watson-Crick base pairs and their associated isostericity matrices. *Nucleic Acids Res.* **2002**, *30*, 3497−3531.
(88) Maity, H.; Baidya, L.; Reddy, G. Salt-Induced Transitions in the Conformational Ensembles of Intrinsically Disordered Proteins. *J. Phys. Chem. B* **2022**, *126*, 5959−5971.
(89) Beveridge, R.; et al. Ion Mobility Mass Spectrometry Uncovers the Impact of the Patterning of Oppositely Charged Residues on the Conformational Distributions of Intrinsically Disordered Proteins. *J. Am. Chem. Soc.* **2019**, *141*, 4908−4918.
(90) Liu, Y.; et al. Single-Molecule Detection of α-Synuclein Oligomers in Parkinson's Disease Patients Using Nanopores. *ACS Nano* **2023**, *17*, 22999−23009.
(91) Byrd, E. J.; Wilkinson, M.; Radford, S. E.; Sobott, F. Taking Charge: Metal Ions Accelerate Amyloid Aggregation in Sequence Variants of α-Synuclein. *J. Am. Soc. Mass Spectrom.* **2023**, *34*, 493−504.
(92) Wang, H.; Wu, J.; Sternke-Hoffmann, R.; Zheng, W.; Mörman, C.; Luo, J. Multivariate effects of pH, salt, and Zn2+ ions on Aβ40 fibrillation. *Commun. Chem.* **2022**, *5*, 171.
(93) Yoshimura, Y.; et al. Distinguishing crystal-like amyloid fibrils and glass-like amorphous aggregates from their kinetics of formation. *Proc. Natl. Acad. Sci. U.S.A.* **2012**, *109*, 14446−14451.
(94) Gaspar, R.; Lund, M.; Sparr, E.; Linse, S. Anomalous Salt Dependence Reveals an Interplay of Attractive and Repulsive Electrostatic Interactions in α-synuclein Fibril Formation. *QRB discov.* **2020**, *1*, No. e2.
(95) Yusko, E. C.; et al. Single-Particle Characterization of Aβ Oligomers in Solution. *ACS Nano* **2012**, *6*, 5909−5919.
(96) Awasthi, S.; Ying, C.; Li, J.; Mayer, M. Simultaneous Determination of the Size and Shape of Single α-Synuclein Oligomers in Solution. *ACS Nano* **2023**, *17*, 12325−12335.
(97) Zhao, C.; et al. DNase-targeted natural product screening based on a sensitive and selective DNase I detecting system. *RSC Adv.* **2017**, *7*, 30911−30918.
(98) Chau, C. C.; Weckman, N. E.; Thomson, E. E.; Actis, P. Solid-State Nanopore Real Time Assay for Monitoring Cas9 Endonuclease Reactivity. *bioRxiv* **2024**, bioRxiv:2024.09.20.612695.

https://doi.org/10.1021/acsnano.4c15173
ACS Nano 2025, 19, 3839−3851